Physics of Plasmas

Statistical investigation of electric field fluctuations around the lower-hybrid frequency range at dipolarization fronts in the near-earth magnetotail

Cite as: Phys. Plasmas **29**, 012111 (2022); https://doi.org/10.1063/5.0067382
Submitted: 16 August 2021 • Accepted: 23 December 2021 • Published Online: 24 January 2022

M. Hosner, R. Nakamura, T. K. M. Nakamura, et al.

Statistical investigation of electric field fluctuations around the lower-hybrid frequency range at dipolarization fronts in the near-earth magnetotail

Cite as: Phys. Plasmas **29**, 012111 (2022); doi: 10.1063/5.0067382
Submitted: 16 August 2021 · Accepted: 23 December 2021 ·
Published Online: 24 January 2022

View Online Export Citation CrossMark

M. Hosner,[1,2,a)] R. Nakamura,[1,2] T. K. M. Nakamura,[2] D. Schmid,[1] E. V. Panov,[1,2] and F. Plaschke[3]

AFFILIATIONS

[1]Space Research Institute, Austrian Academy of Sciences, 8042 Graz, Austria
[2]Institute of Physics, Graz University, 8010 Graz, Austria
[3]Institute of Geophysics and Extraterrestrial Physics, Technische Universität Braunschweig, 38106 Braunschweig, Germany

Note: This paper is a part of the Special Collection: Plasma Physics from the Magnetospheric Multiscale Mission.
[a)]**Author to whom correspondence should be addressed:** martin.hosner@oeaw.ac.at

ABSTRACT

Dipolarization fronts (DFs) are thin magnetic boundary structures, embedded in short-duration, fast earthward-moving plasma flows, so-called bursty bulk flows. Previous case studies have shown that the density gradient at DFs can excite the lower-hybrid drift instability (LHDI) and resulting kinetic-scale waves. These waves feature strong electric field fluctuations perpendicular to the ambient magnetic field and associated effective particle acceleration/heating. In this study, we statistically examine electric field fluctuations in the lower-hybrid (LH) frequency range of 61 DF events, using data from the Magnetospheric Multiscale (MMS) Mission between 2017 and 2018 when the MMS apogee was in the magnetotail. We observed that all DF events exhibit enhanced power in the electric field fluctuations in the LH frequency range. Among the observed events, the power can vary by several orders of magnitude. The waves are detected for both high and low values of the perpendicular electron density or pressure gradient. In addition, the peak wave power within the DF is often observed at the time of steepest density gradient within the DF. The results also reveal that the wave power correlates with the magnetic flux transport rate of the DFs. These findings suggest that enhanced density and pressure gradients, which can be formed by large-scale flux transport at DFs, lead to LHDI-related kinetic-scale wave signatures at the DFs, and this may modify the original gradient layer profile of the DF in the course of its propagation from the source to the observation point.

I. INTRODUCTION

Bursty bulk flows (BBFs) in the earth's magnetotail (Baumjohann *et al.*, 1990; Angelopoulos *et al.*, 1992), which are considered as a result of magnetic reconnection (Baumjohann, 2002; Nagai and Machida, 1998), are responsible for an effective plasma and magnetic flux transport across the magnetotail toward earth. In the dawn–dusk direction, they exhibit typical sizes of 2–3 R_E and a vertical extension of 1.5–2 RE (Nakamura *et al.*, 2004). Embedded into BBFs are so-called dipolarization fronts (DFs) (Nakamura *et al.*, 2002), which are understood as propagating, transient magnetic boundary structures with velocities in the range of several hundred km/s (Runov *et al.*, 2009). In spacecraft measurements, they are identified by a sharp increase in the B_z magnetic field component in Geocentric Solar Magnetic (GSM) coordinates (Runov *et al.*, 2009), often preceded by a small dip in the B_z component (Shiokawa *et al.*, 2005; Schmid *et al.*, 2019b) and followed by a longer structure of increased B_z, termed the flux pileup region (Khotyaintsev *et al.*, 2011) or dipolarizing flux bundle (Liu *et al.*, 2013). Dipolarization fronts are structures at scales comparable to the ion inertial length, separating cold, dense plasma ahead from the hotter but diluted plasma within the trailing flux bundle (Sergeev *et al.*, 2012). They are therefore naturally accompanied by a sharp density gradient. Using global hybrid simulations, Lu *et al.* (2015) studied the evolution of DFs over the course of their propagation; they considered the DFs as earthward-propagating flux ropes, originating from a near-earth reconnection site, and were able to explain many typical observed features of DFs such as the sharp B_z enhancement, small-amplitude preceding dips in the B_z component, dawn-duskward electric field signatures, and enhanced earthward flow. On electron scales, dipolarization fronts were studied using data from the Magnetospheric Multiscale (MMS) Mission (Burch *et al.*, 2016) by Liu *et al.* (2018), who reported strong perpendicular currents in the low-density region of the DF and identified the DF as a region of mostly positive $\mathbf{j} \cdot \mathbf{E}$. MMS provides high-time resolution plasma measurements and is therefore particularly suitable for the study of electron/ion scale-related phenomena. It was launched in 2015 and features four spacecraft, which are separated by distances at the range of the electron to ion scale. Dipolarization fronts are hosts of various energy conversion processes (Angelopoulos *et al.*, 2013; Khotyaintsev *et al.*, 2017; Malykhin *et al.*, 2019; Birn *et al.*, 2013; Smets *et al.*, 1999; Lu *et al.*, 2016; Wu *et al.*, 2013; Huang *et al.*, 2015), effectively heating and accelerating electrons and ions.

At dipolarization fronts, various types of instabilities on different scale sizes were observed, e.g., the ballooning/interchange instability (e.g., Lapenta and Bettarini, 2011) on ion scales and the lower-hybrid drift instability (LHDI), which develops at electron-kinetic scales (Krall and Liewer, 1971; Davidson and Gladd, 1975) and hybrid-kinetic scales (Daughton, 2003). The LHDI becomes unstable due to present density gradients and associated diamagnetic currents (Davidson and Gladd, 1975). It was demonstrated that the LHDI develops at the front region when large density gradients are established and that the growth of the electric field amplitude and the density gradient are linked (Nakamura *et al.*, 2016). Electric field fluctuations in the lower-hybrid frequency range, perpendicular to the ambient magnetic field, were interpreted as a result of the LHDI in *in situ* measurements (Zhou *et al.*, 2009; Divin *et al.*, 2015a; Contel *et al.*, 2017) and simulations (Divin *et al.*, 2015b). As such, the LHDI and the associated waves play an important role for electron acceleration (Cairns and McMillan, 2005) and ion heating (Greco *et al.*, 2017) at DFs. Single-event observations (Pan *et al.*, 2018) as well as simulations (Nakamura *et al.*, 2019) have further shown that the LHDI can be responsible for ripple-like disturbances of parameters such as the magnetic field and density at the DF front region on electron-kinetic scales. Furthermore, Nakamura *et al.* (2019) also presented results about LHDI growth rates by combining fully kinetic simulations and a linear dispersion relation solver in the fully kinetic regime, showing that the timescale of the fastest growing mode of the LHDI is in the range of seconds under realistic conditions.

Despite these results, the typical temporal evolution of LHDI-associated electric field fluctuations during the dipolarization front as they propagate earthward is not yet fully understood. Furthermore, due to the mentioned short growth timescales, it is difficult to make statements about the elapsed time and stage of the LHDI itself. This study aims to contribute to a better understanding of the conditions under which the LHDI can be observed by analyzing a larger number of events, using data from the MMS mission. Here, for the first time, we present a statistical analysis of observational data that comprise of DF events, among which the power of the LHDI-associated waves varies by several orders of magnitude. In this work, a link between a present electron density/pressure gradient across DFs and lower-hybrid wave signatures, which are interpreted as a result of the LHDI, is investigated. We make statements about the prevalence of perpendicular electric field fluctuations in the lower-hybrid frequency range, relate the measured wave power to ambient plasma parameters, and provide parameter ranges in which such fluctuations can be expected or not. Furthermore, we assess the question where such waves appear in relation to the DF structure onset/end and to the density gradient, and discuss possible reasons and mechanisms that can be responsible for stronger/weaker waves at DFs.

II. METHODOLOGY

A. Event selection and database

For the investigation, we use data from the Magnetospheric Multiscale (MMS) Mission (Burch *et al.*, 2016). We use the initial database from Schmid *et al.* (2019b), comprising 203 events but select only events that were obtained during June, July, and August of 2017 and 2018 when the apogee of MMS was clearly in the magnetotail.

For single-spacecraft analysis techniques, we use burst mode data from MMS1; therefore, all events are discarded where high-time resolution burst data of MMS1 are not available or degraded. This results in a subset of 86 DF candidates. Among these candidates, a subsequent selection is performed, based on magnetic properties. The 86 events are checked for fulfilling the following criteria, using survey mode data of the flux gate magnetometer (Russell *et al.*, 2016) of MMS1:

- Transient events: the duration of the DF, Δt_{DF}, which is defined as the time between minimum and maximum B_z, must not exceed 10 s.
- Dipolarization: $\Delta B_z > 5$ nT within Δt_{DF}.
- Change of magnetic field orientation: the change in elevation angle (Baumjohann *et al.*, 1999) must be greater than 10°, i.e., $\theta = \arctan\left(\frac{B_z}{\sqrt{B_x^2+B_y^2}}\right) > 10°$.
- Final magnetic field orientation: the elevation angle at the DF end time (i.e., time of maximum B_z) must exceed $\theta > 40°$.
- Proximity to central plasma sheet is required to ensure that the spacecraft crosses at the DF center: $\mathrm{median}(B_x) < 10$ nT within 60 s before the DF.

Among the events in the subset, a total amount of 61 events fulfill these criteria and are further considered. The range of characteristic parameters of all 61 events is summarized in Table I. On average, the thickness of an entire DF is therefore in the range of several ion inertial lengths for all the considered events; however, the DF can contain substructures with enhanced density gradients at which the ions can be unmagnetized. A spatial overview of all events is displayed in Fig. 1, which shows all events in the X/Y plane in Geocentric Solar

TABLE I. Parameter range of the 61 DF events that provide the dataset of this study. The median and the upper and lower quartiles are given for the plasma beta before the DF β, the thickness of the DF, normalized by the ion inertial length d_{DF}/d_i, the DF timing velocity v_t, the electron density before the DF n_e, and the total ion bulk velocity at the DF v_i. Here, the term before the DF refers to the time interval of length Δt_{DF} before the DF onset.

	β	d_{DF}/d_i	v_t(km/s)	n_e (cm^{-3})	v_i (km/s)
Max	479	7.59	887	2.12	614
Upper quartile	57	4.02	400	0.54	329
Median	26	3.44	302	0.31	287
Lower quartile	15	2.42	268	0.20	216
Min	2	1.16	146	0.08	113

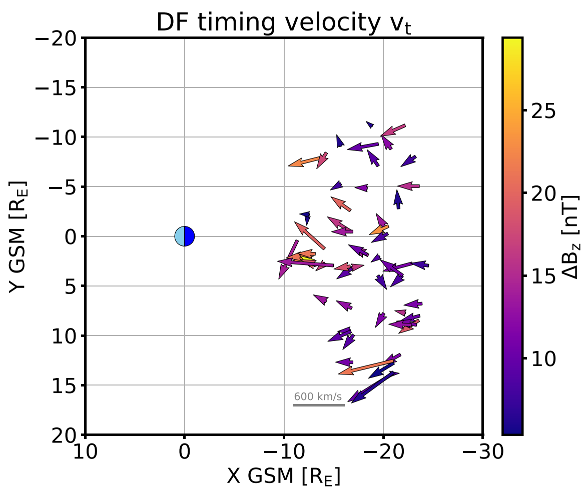

FIG. 1. An overview of the 61 events that match the selection criteria. The colors represent the change in the northward magnetic field component during the DF, ΔB_z, and the arrows represent the DF propagation direction perpendicular to the boundary (obtained by the timing method), projected onto the X/Y plane in GSM.

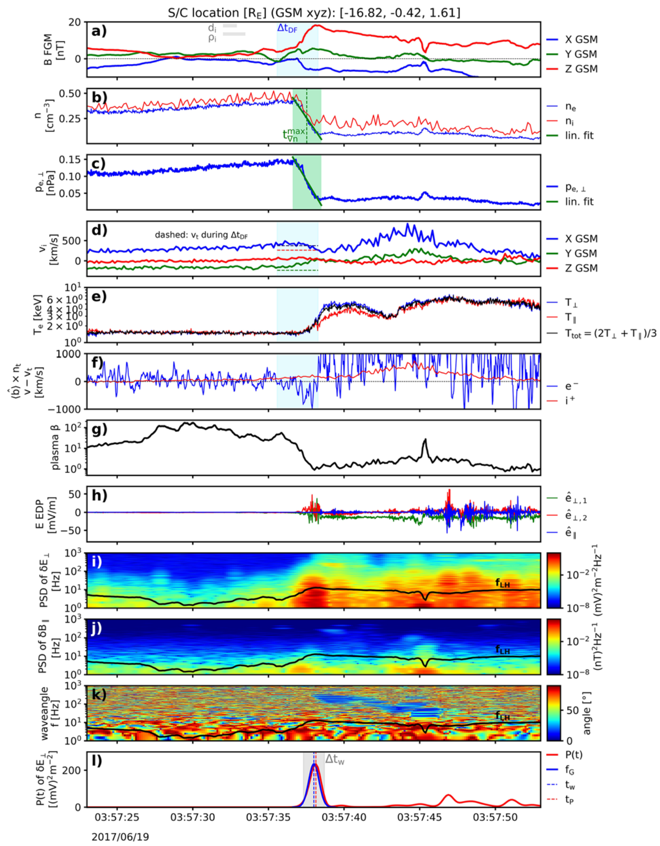

FIG. 2. In panel (a), the ambient magnetic field is shown and the time interval of the dipolarization front with the duration Δt_{DF} is highlighted by the blue region. As a reference, the ion inertial length d_i and the ion gyroradius ρ_i are shown as gray bars at the DF. In panel (b), the electron and ion densities are shown together with the gradient region highlighted in green and the fitted electron density. The green dashed line shows the time of steepest electron density gradient, $t_{\nabla n}^{max}$. In panel (c), the perpendicular electron pressure $p_{e,\perp}$ together with a linear fit of $p_{e,\perp}$ from within the gradient range (green highlighted region) is shown. The ion bulk velocity v_i in GSM coordinates is shown, together with the DF propagation velocity v_t in panel (d). In panel (e), the parallel, perpendicular, and total electron temperatures are shown. In panel (f), v_i and v_e in the co-moving frame are shown in the direction tangential to the DF, $(\langle \hat{b} \rangle_{\parallel} \times n_t)$. The plasma β is shown in panel (g), the electric field fluctuations in the field-aligned coordinate (FAC) system are shown in panel (h). In panels (i) and (j), the Power Spectral Densities (PSDs) of the perpendicular components of E, and the parallel component of B, together with the lower-hybrid frequency in black, are shown. Panel (k) shows the angle between the ambient magnetic field and the wave vector $\mathbf{k}$. Panel (l) shows the integrated PSD, P, in red as well as the time of maximum wave power t_P as the red dashed line. The blue solid line represents a Gaussian function f_G centered around t_w (blue dashed line), which is the power-weighted average time where wave signatures occur. All timestamps are given in UTC.

Magnetospheric (GSM) coordinates. The GSM system has its origin at the center of the earth and it is defined such that the x_{GSM} component points toward the sun, z_{GSM} aligns with the magnetic dipole axis but is projected such that it is perpendicular to x_{GSM}, and y_{GSM} completes the right-handed system such that $x_{GSM} \times y_{GSM} = z_{GSM}$ is fulfilled. The arrows represent the direction $\mathbf{n}_t$ and velocity v_t of propagation of the DF structures, normal to the boundary and projected onto the X/Y plane, obtained by the timing method (Harvey, 1998; Plaschke *et al.*, 2016). The color represents ΔB_z, i.e., the difference in the B_z component between the beginning and end time of the DF. In Fig. 2, the parameters of a typical DF event are shown, which are used for the analysis. Figure 2(a) displays the magnetic field from the flux gate magnetometer in GSM coordinates, in which the blue region highlights the DF time range Δt_{DF} and the gray lines depict the ion inertial length d_i and the ion gyroradius ρ_i as a reference. The characteristic increase in the B_z component of the magnetic field is visible during the DF. In Fig. 2(b), the electron and ion densities are shown together with the electron density gradient range (green region) and a linear fit of the electron density signal (green line). The time of steepest gradient $t_{\nabla n}^{max}$ is marked by a dashed green line. Here, a clear decrease in n_e and n_i is visible across the DF. In Fig. 2(c), the perpendicular electron pressure is shown. The green line represents a fitted linear function to the $p_{e,\perp}$ data out of the gradient region, which is highlighted in green. Similar to the density, a pressure decrease is observed across the front. In Fig. 2(d), the ion bulk velocity v_i is shown in GSM coordinates. The dashed lines during the DF time interval represent the DF propagation velocity along its normal direction $\mathbf{v}_t$. Both the DF velocity and the ion flow velocity are almost the same, indicating that the DF structure is embedded into the earthward ion flow. Figure 2(e) shows the parallel, perpendicular, and total electron temperatures. Toward the end of the DF structure, a moderate increase in both the perpendicular and parallel electron temperature is observed. However, the strongest increase in temperature, accompanied by a temperature anisotropy ($T_\parallel < T_\perp$), is observed mainly behind the DF event, which is consistent with findings by Khotyaintsev *et al.* (2011), who attributed such observations to whistler wave modes. Figure 2(f) highlights $v_i - v_t$ and $v_e - v_t$, i.e., the ion and electron velocity in the co-moving frame with respect to the DF, but in coordinates that are aligned with the boundary. In particular, we show the components of the ion and electron flow tangential to the boundary, i.e., in the direction of $\langle \hat{b} \rangle \times \mathbf{n}_t$, where $\langle \hat{b} \rangle$ denotes the unit vector in the direction of the average background magnetic field during the DF time interval and $\mathbf{n}_t$ denotes the unit vector of the boundary normal, $\mathbf{n}_t = \mathbf{v}_t/v_t$. Toward the end of the DF time interval, the electron flow velocity mostly exceeds the ion flow velocity, indicating that the current tangential to the boundary is mostly carried by electrons. Figure 2(g) shows the plasma beta. Values in the range between 10 and 100 before the DF and values in the range around 1 after the DF suggests that the event acts as a boundary between a thermal pressure-dominant plasma sheet and a more diluted plasma region with stronger magnetic pressure behind the DF. In Fig. 2(h), the components of the electric field are shown in field-aligned coordinates (FACs). During the DF, the dominant fluctuations are observed to be perpendicular to the ambient magnetic field. Figure 2(i) shows the power spectral density (PSD) of the perpendicular electric field fluctuations $\delta E_\perp$ and the lower-hybrid frequency $f_{\rm LH}$ as a black line. At the front region, the highest power is observed in the range around $f_{\rm LH}$ and below. In Fig. 2(j), the PSD of the magnetic field fluctuations, parallel to the background magnetic field, is shown. Signatures of enhanced power are observed in the same frequency region and time as in the electric field fluctuation PSD. Figure 2(k) shows the angle spectrum between the background magnetic field and the wave propagation vector **k**, obtained by the method by Means (1972). At the DF region around the lower frequency, the angle of the wave vector predominantly assumes values toward 90°. Figure 2(l) shows the integrated PSD over the frequency, P, as the red solid line. The time range of the observed fluctuations Δt_w is indicated by the gray highlighted region. The time point of maximum power, t_P, is indicated by a red dashed line. The blue solid line represents a Gaussian function f_G that acts as a proxy for the observed wave power and is used in the analysis to describe the temporal properties of the observed fluctuations. Its height corresponds to the maximum integrated power and its width is linked to the total energy of the observed fluctuations. The time point of the center of f_G is represented by a blue dashed line and is denoted by t_w. It is determined by the weighted average time of the integrated wave power P. Further details about obtaining P as well as about the construction of f_G are given in Sec. II B.

B. Analysis

For the single-spacecraft analysis techniques, we use data from MMS1. Unless otherwise noted, burst mode data from the FGM instrument is used, which features a sample rate of 128 Hz. We further use burst mode data of the Fast Plasma Investigation (FPI) (Pollock *et al.*, 2016) for plasma moments such as electron and ion density, bulk velocity, and pressure. In the burst mode, the sample rate is 33.3 Hz for electron moments and 6.6 Hz for ion moments, respectively. For the electric field fluctuation δE analysis, we use burst mode data from the electric double probe (EDP) instrument (Lindqvist *et al.*, 2016) with a sample rate of 8192 Hz. For the calculation of the magnetic field power spectrum as well as for the wave propagation direction, we use burst mode data from the Search Coil Magnetometer (SCM) (LeContel *et al.*, 2016) with a sample rate of 8192 Hz. For all the DF events, the boundary normal propagation velocity v_t and normal propagation direction $\mathbf{n}_t$ are determined using the timing method (Harvey, 1998; Plaschke *et al.*, 2016) on survey mode magnetic field data from the FGM instrument of MMS1–4, which features a sample rate of 16 Hz. For the events of the used database (47 out of 61 events), the boundary normal vectors point at angles around $90.1° \pm 6.0°$, relative to the average ambient magnetic field during the DF time interval and are, therefore, considered perpendicular to the boundary.

To categorize and quantify electric field fluctuations at the DF, burst mode data of the electric field **E** from EDP are transformed into a field-aligned coordinate (FAC) system $(\mathbf{e}_\parallel, \mathbf{e}_{\perp,1}, \mathbf{e}_{\perp,2}) = (\mathbf{b}, \mathbf{v}_i \times \mathbf{b}, \mathbf{b} \times (\mathbf{v}_i \times \mathbf{b}))$. Here, **b** denotes the unit vector of the total magnetic field from FGM and $\mathbf{v}_i$ the ion bulk velocity unit vector. We do not take the average of **b** and $\mathbf{v}_i$ but instead supersample to the time base of E and calculate the orientation of the FAC for each data point of E. The power spectral density (PSD) is estimated for each component of **E** in the FAC from the squared Fourier transformed signal. We take $S = S_{E,\perp,1} + S_{E,\perp,2}$ to be the PSD of the perpendicular components of **E** and it is represented by the sum of PSDs of each perpendicular component [see Fig. 2(g)]. Here, we solely focus on the electric field component, perpendicular to the ambient magnetic field, since the lower-hybrid wave features a dominant perpendicular electric field component in the frequency range below and around the lower-hybrid frequency $f_{\rm LH} \approx \sqrt{f_{ce} f_{ci}}$ with f_{ce} and f_{ci} being the electron and ion gyrofrequencies, respectively. Furthermore, any contributions from Whistler wave modes, which can be identified by propagation directions parallel to the background magnetic field, and are also commonly observed at dipolarization fronts (Viberg *et al.*, 2014; Huang *et al.*, 2012), must be excluded. At DFs, Whistler modes are predominantly found behind the DF structure after the B_z maximum, within the dipolarizing flux bundle, and are accompanied by a temperature anisotropy, i.e., with $T_\perp/T_\parallel > 1$ (Malykhin *et al.*, 2021; Khotyaintsev *et al.*, 2011). Also, we acknowledge that Whistler modes can also be found at $f < f_{\rm LH}$; however, the majority is observed in the frequency range $f_{\rm LH} < f < f_{ce}$ (Liang *et al.*, 2012; Grigorenko *et al.*, 2020; Malykhin *et al.*, 2021). Figure 2(k) indicates mostly perpendicular propagation directions. For the analysis, we, therefore, use the simple approach of excluding all contributions above the lower-hybrid frequency. With this motivation, we use a modified power spectrum, that is,

$$S_m(t,f) = \begin{cases} 0 & f < 2\,\mathrm{Hz}, \\ S(t,f) & 2 \le f \le f_{\rm LH}, \\ S(t,f)\exp\left(-\dfrac{f - f_{\rm LH}}{f_{\rm LH}}\right) & f > f_{\rm LH}. \end{cases} \quad (1)$$

We exclude the wave power from convective E field contributions in the observer frame as well as Alfvénic signatures by setting the lower integration limit to 2 Hz. To gradually exclude frequency contributions above $f_{\rm LH}$, we modify S with an exponential. Here, $f_{\rm LH}$ is constant and set to the maximum lower-hybrid frequency during the DF. In Fig. 3, we show the averaged power spectrum of the perpendicular electric field fluctuations of a DF event at UT 2017-06-19/03:57:38 for demonstration. It is averaged over a time interval of width Δt_w that is centered around the average time of strongest wave power t_w. It is visible that in the frequency range of interest (blue shaded range), the power of the perpendicular electric field fluctuations is enhanced.

To exactly determine the beginning and ending times of the DF, we apply an automated search algorithm. We use the 16 Hz survey-mode FGM magnetic field data out of a 40 s time window, which starts 10 s before the DF onset, which was identified by Schmid *et al.* (2019a). First, the signal is smoothed, using a sliding window of 0.5 s width. We then search the B_z component for all minima and maxima,

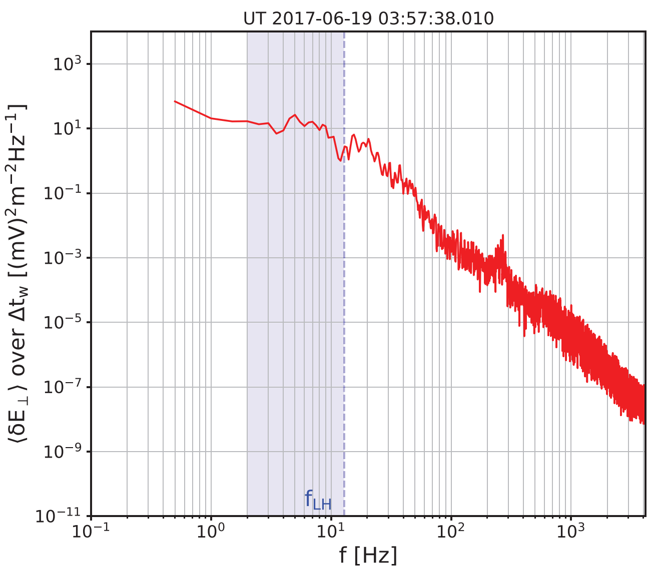

FIG. 3. Power spectrum of the perpendicular electric field fluctuations of the event at UT 2017-06-19/03:57:38. The spectrum is averaged over all time points of an interval of width Δt_w, which is centered around the average time of strongest wave power t_w. The blue shaded area illustrates the frequency range between 2 Hz and f_{LH}. An enhancement of wave power in this interval is visible.

which serve as potential DF beginning and ending time candidates of the DF, respectively. Then, all minima/maxima combinations are checked to see if they fulfill the criteria of Sec. II A. For all passing combinations, we further calculate the time difference Δt and northward magnetic field difference ΔB_z. We choose the combination of time points with highest $\Delta B_z/\Delta t$ for the beginning and ending time of the DF, respectively, to capture the steep B_z increase region of the DF. Consequently, the DF beginning and end times are denoted by $t_{\rm Bz}^{\rm min}$ and $t_{\rm Bz}^{\rm max}$, respectively, and the DF duration is $\Delta t_{\rm DF} = t_{\rm Bz}^{\rm max} - t_{\rm Bz}^{\rm min}$. The total power of the present fluctuations [Fig. 2(h)] is calculated by

$$P(t) = \int S_m(t,f)\, df. \qquad (2)$$

To obtain the electron density and pressure gradient across the DF, burst mode FPI moments are used. It is expressed as follows:

$$\nabla n_{e,\perp} = -\frac{dn_e}{dt}\frac{1}{v_t}, \qquad (3)$$

with v_t being the DF propagation velocity. The time derivative term is determined by first identifying the time range over which the density decreases and then performing a linear fit to the density signal. Since the density typically decreases across the front, a negative sign is added to obtain positive values for the density gradient. The perpendicular electron pressure gradient $\nabla p_{e,\perp} = -(dp_{e,\perp}/dt)(1/v_t)$ is determined accordingly. Note that we do not use multi-spacecraft methods to determine the density gradient because FPI burst mode data are not available for all four MMS spacecraft for events in 2018.

During the DF crossing, the wave power $P(t)$ does not always show as a single peak with one distinct maximum but can have more than one maximum or no maximum. It is, therefore, not straightforward to define the time of strongest wave power and wave duration. Instead, we construct a Gaussian function $f_G(t) = a\exp\left(-(t-t_w)^2/2c^2\right)$ as a proxy for the real P, associated with the DF. It is constructed such that a is set to the maximum P within the examined time window and it must furthermore fulfill

$$\int_{\Delta t_{\rm DF}^{\rm ext}} P(t)dt = \int_{-\infty}^{\infty} a\exp\left(-\frac{(t-t_w)^2}{2c^2}\right)dt, \qquad (4)$$

that is, the energy is conserved. From Eq. (4), the width of the function f_G in the time domain, denoted by c, is calculated, and we interpret $\Delta t_w = 4c$ as the wave duration. This proxy function is centered around $t_w = \int P(t)tdt/\int P(t)dt$. Here, t_w represents the center time point of the wave signatures during the DF and is defined as the power-weighted average time where wave signatures occur during the DF. For all the events, we consider a symmetrically extended time interval around the DF front, $\Delta t_{\rm DF}^{\rm ext} = 1.20\Delta t_{\rm DF}$ in order to take the uncertainty in finding $t_{\rm Bz}^{\rm min}$ and $t_{\rm Bz}^{\rm max}$ into account.

To measure the strength of the obtained fluctuations of $\delta E_\perp$, we define $\langle P\rangle_{\rm sig}$ as the average wave power in the time interval $t_w \pm 2c$, i.e., during the dwell time of the wave. To quantitatively investigate the prevalence of waves at DF structures and the influence thereof, we compare the wave power during the DF event with the wave power before. We introduce the average wave power during the DF time, which is $\langle P\rangle_{\rm DF} = (1/\Delta t_{\rm DF})\int_{\rm DF} P(t)\, dt$. Here, the subscript indicates that the integration is performed over the DF time interval. We compare this to the wave power before the DF, $\langle P\rangle_{\rm bef}$, which is defined in a similar way to $\langle P\rangle_{\rm DF}$, but we consider the time interval of one DF duration before the front onset: $t_{\rm Bz}^{\rm min} - \Delta t_{\rm DF} \le t \le t_{\rm Bz}^{\rm min}$. Accordingly, the average wave power after the front, i.e., in the dipolarizing flux bundle, is denoted by $\langle P\rangle_{\rm aft}$ and is obtained by considering $t_{\rm Bz}^{\rm max} \le t \le t_{\rm Bz}^{\rm max} + \Delta t_{\rm DF}$.

III. RESULTS

Motivated by the density gradient, being the driver of the LHDI (Davidson *et al.*, 1977), we aim to compare the density gradient and lower-hybrid wave properties. Figure 4 shows the time evolution of $\nabla n_{e,\perp}$ in panel (a) and the wave power $P(t)$ in panel (b) for each event. In order to be able to compare the time properties among different events, we introduce an alternative time axis for all events, i.e., we map the time axis of each event to a generalized time coordinate t_r. We rescale the time vector of each event by its respective $\Delta t_{\rm DF}$ and shift the time axis such that the start time of the DF corresponds to the origin, i.e., $t_{\rm Bz}^{\rm min}$ corresponds to $t_r = 0$. Due to the normalization by $\Delta t_{\rm DF}$, the DF end time $t_{\rm Bz}^{\rm max}$ corresponds to $t_r = 1$. Furthermore, for each event the density gradient and the wave power are normalized by their respective maxima from within a time interval between $-1 < t_r < 2$, which corresponds to $t_{\rm Bz}^{\rm min} - \Delta t_{\rm DF} < t < t_{\rm Bz}^{\rm max} + \Delta t_{\rm DF}$. The 61 events are ordered based on $|t_{\nabla n}^{\rm max} - t_P|/\Delta t_{\rm DF}$, i.e., the relative temporal deviation between the time of the steepest density gradient $t_{\nabla n}^{\rm max}$ and the time of maximum wave power t_P, obtained within the shown interval $-1 < t_r < 2$. Based on this ordering, we assign a number to each event.

We validated the beginning/end times of the DF and the $n_{e,\perp}$ gradient region by visual inspection. The DF beginning/end times were found to be reasonable for all events, except for events No. 50, 51, 53, 54, 57, 58, 59, 60. The $\nabla n_{e,\perp}$ region was found to be reasonable for all events, except for event No. 48, 49, 51, 52, 53, 54, 55, 56, 57, 58, 59, 60, 61. All the events for which both the beginning/end times of the density gradient as well as the DF are determined correctly by the

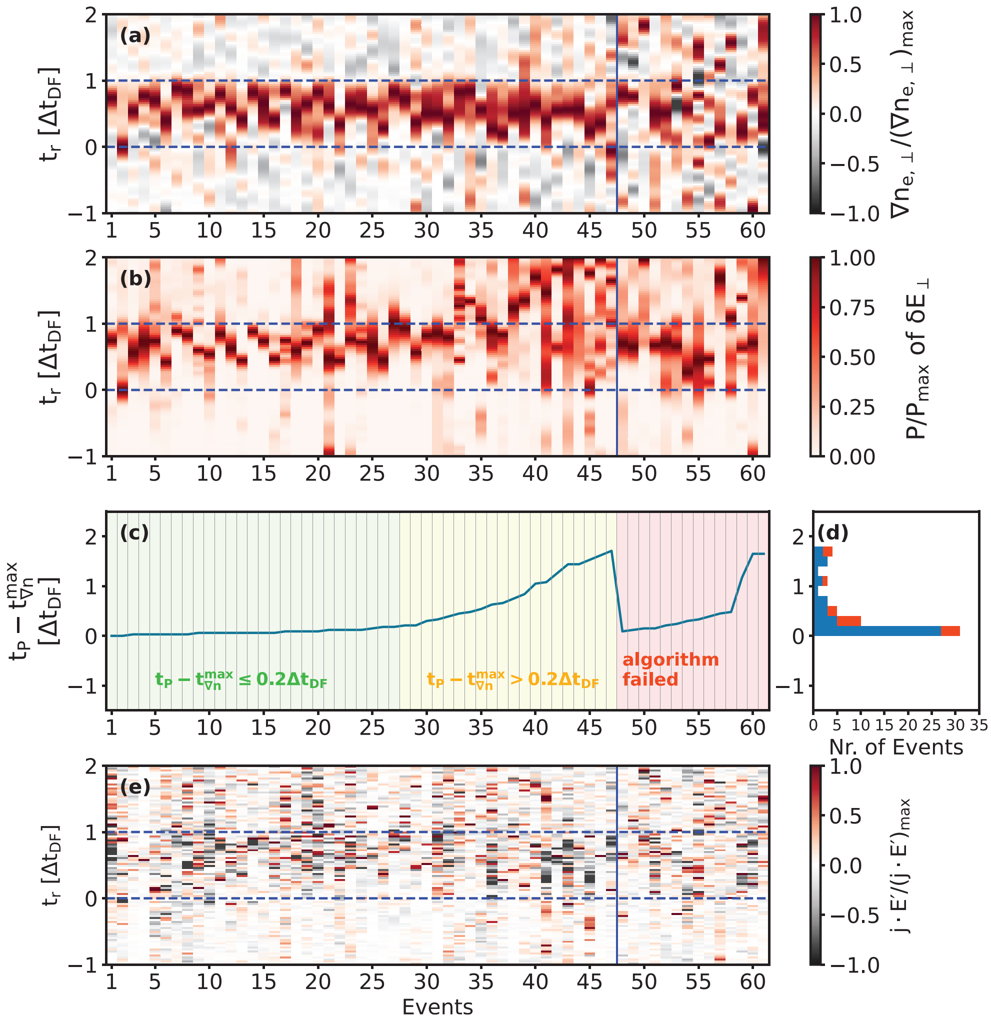

FIG. 4. (a) Time evolution of $\nabla n_{e,\perp}$ for each event in the generalized time coordinate t_r on the vertical axis. The displayed time range encompasses $-1 \leq t_r \leq 2$ and therefore corresponds to $t^{min}_{Bz} - \Delta t_{DF} < t < t^{max}_{Bz} + \Delta t_{DF}$ for all events. Time progresses from bottom to top. Red indicates a decreasing density across the front and black indicates an increasing density. Panel (b) shows the wave power P in the same way. To be able to compare different events, P and $\nabla n_{e,\perp}$ are both displayed normalized by their respective maximum/steepest gradient values from within $-1 \leq t_r \leq 2$. (c) Time difference between the time of steepest density gradient $t^{max}_{\nabla n}$ and the maximum wave power t_P in units of one DF duration Δt_{DF}, taken from the shown interval of $-1 \leq t_r \leq 2$. The color shading represents the different categories. (d) A histogram of all events. The events are binned by the deviation $|t_P - t^{max}_{\nabla n}|$; panels (c) and (d) share the vertical axis. (e) Normalized $\mathbf{j} \cdot \mathrm{E}'$ in the electron frame.

automated method are taken into account in the results (event No. 1–47). Events for which the automated method failed for at least the DF or $\nabla n_{e,\perp}$ beginning/end times are marked as a separate category (event No. 48–61). Events for which the density gradient region was not determined correctly, no statement about $\nabla n_{e,\perp}$ values is made.

First, we highlight that enhancement of the wave power is observed at all 47 events, in general, in the middle or toward the end of the respective events. The density gradient region is generally confined within the DF interval. It is shorter or comparable to Δt_{DF} and the steepest density gradient is found within the DF time interval. Second, when comparing panel Figs. 4(a) and 4(b), we observe that the time of the steepest density gradient $t^{max}_{\nabla n}$ is temporally aligned with the time of maximum wave power, t_P, for a large part of the considered events (57%). In Fig. 4(c), the temporal deviation $|t^{max}_{\nabla n} - t_P|/\Delta t_{DF}$ is shown for each event. We observe that for event No. 1–27, the deviation is small ($|t^{max}_{\nabla n} - t_P|/\Delta t_{DF} \leq 20\%$), indicating a strong temporal alignment between the steepest density gradient and strongest wave power. For higher event numbers, the deviation increases up to almost $2\Delta t_{DF}$. This is further quantitatively illustrated in a histogram, which bins the number of events by $|t^{max}_{\nabla n} - t_P|/\Delta t_{DF}$ in Fig. 4(d). Based on this observation, the events 1–27 ($27/47 = 57\%$ of considered events, $27/61 = 44\%$ of the total database) are marked as category 1 (green) and events 28–47 ($20/47 = 43\%$ of considered events, $20/61 = 33\%$ of the total database) as category 2 (yellow, represents events with $|t^{max}_{\nabla n} - t_P|/\Delta t_{DF} > 20\%$). The remaining events 48–61 ($14/61 = 23\%$ of the total database) are marked as category 3 (red). It should be noted, however, that some of the events in category 2 show more than one peak in the wave power. Among those local peaks in the wave power, one can

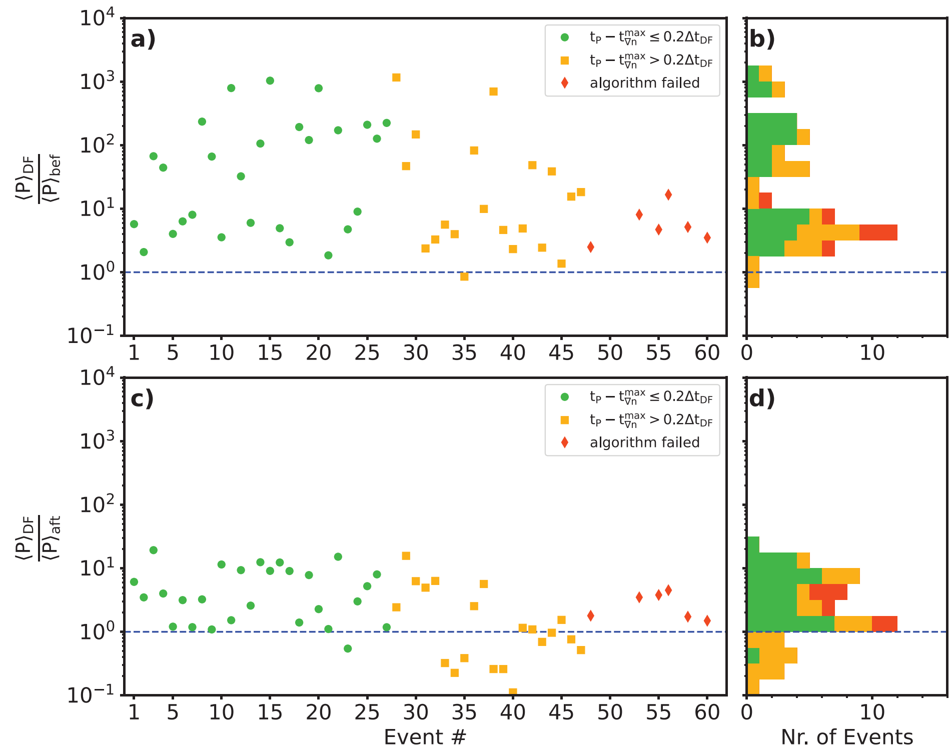

FIG. 5. (a) The power ratio of the wave during/before the dipolarization front $\langle P\rangle_{DF}/\langle P\rangle_{bef}$. (b) The events are binned with respect to the power ratio and displayed as a histogram. The number of events in each category are stacked, i.e., the total bar length indicates the total number of events in one respective bin. The bin limits are of equal distance in logarithmic space and such that each decade features four bins. Panels (c) and (d) are similar to panels (a) and (b) but show the ratio between the wave power during/after the DF, $\langle P\rangle_{DF}/\langle P\rangle_{aft}$. The colors represent category 1 (green) and category 2 (yellow) events, the red points represent events for which the determination of the $\nabla n_{e,\perp}$ region failed.

still be temporally aligned with the time of steepest density gradient. However, since it is not the global maximum peak, it leads to an overestimated temporal deviation of $|t_{\nabla n}^{max} - t_P|/\Delta t_{DF}$.

In Fig. 4(e), $\mathbf{j}\cdot\mathbf{E}'$ in the electron co-moving frame is shown. The calculation of $\mathbf{j}\cdot\mathbf{E}' = \mathbf{j}\cdot(\mathbf{E}+\mathbf{v}_e\times\mathbf{B})$ is performed by using the curlometer technique (Dunlop *et al.*, 2002) to calculate the current density $\mathbf{j}$ and then taking $\mathbf{E}$, $\mathbf{v}_e$, and $\mathbf{B}$ at the barycenter of the spacecraft tetrahedron. Events for which burst data are not available from all four spacecraft, $\mathbf{E}$, $\mathbf{v}_e$, and $\mathbf{B}$ are instead used from MMS1 only. The highest magnitudes of $\mathbf{j}\cdot\mathbf{E}'$ are generally found to occur during the DF time interval.

In Fig. 5, we compare the average wave power during the DF with the average wave power before and after the DF. Note that, due to the above given definition of $\langle P\rangle_{DF}$, $\langle P\rangle_{bef}$, and $\langle P\rangle_{aft}$, the ratio of the average power also represents the ratio of total wave energies in the respective time intervals. In Fig. 5(a), the ratio between the wave power during/before the DF is displayed for all events. In general, the wave power during the DF is dominant compared to the time before the DF onset. In Fig. 5(b), a histogram shows the distribution of the events over the power ratio $\langle P\rangle_{DF}/\langle P\rangle_{bef}$, indicating that category 1 events exhibit slightly higher ratios compared to category 2 events [the median value (upper, lower quartile) of $\langle P\rangle_{DF}/\langle P\rangle_{bef}$ for Cat. 1: 44.3 (181.9, 5.3), and for Cat. 2: 7.8 (47.2, 3.1)]. In Fig. 5(c), a comparison of the average wave power during the DF/after the DF is displayed. It is indicated that category 1 events exhibit, in general, stronger wave signatures during the DF, whereas for category 2 events the ratio is on average lower, i.e., wave signatures can also be observed behind the DF [the median value (upper, lower quartile) of $\langle P\rangle_{DF}/\langle P\rangle_{aft}$ for Cat. 1: 3.5 (9.1, 1.5), and for Cat. 2: 1.0 (3.1, 0.4)]. In Fig. 5(d), a histogram of the total number of events per power ratio bin is shown, indicating that category 1 events generally feature the strongest wave power during the DF.

Next, we investigate the relation of the wave power with the ambient plasma parameters. The results of a cross correlation analysis are presented in this section and summarized in Table II, which represents the Spearman rank correlation coefficients of the respective quantities. We choose the Spearman rank coefficient over the classic Pearson correlation coefficient because we do not assume a linear relationship and/or normal distribution of the observed quantities. The table shows the coefficient for the combined category 1 and 2 dataset. A weak correlation of the wave power $\langle P\rangle_{sig}$ with the $\nabla n_{e,\perp}$ (0.41) as well as the $\nabla p_{e,\perp}$ (0.46) can be observed. The relation of $\langle P\rangle_{sig}$ to $\nabla n_{e,\perp}$ is shown in Fig. 6(a). Despite considerable scatter, we recognize that $\langle P\rangle_{sig}$ increases with $\nabla n_{e,\perp}$. However, a large wave power is not only observed at large values of $\nabla n_{e,\perp}$ but also at moderate density gradients around 0.2×10^{-3} cm^{-3} km^{-1}. In Fig. 6(c), the wave power is compared to the electron pressure gradient across the front, $\nabla p_{e,\perp}$. Generally, we observe the strongest wave power at strong electron

TABLE II. Spearman rank correlation coefficient of the average wave power with various parameters and gradients across the DFs for category 1 and 2 events. Here, B_z^{max} denotes the magnetic field z component at the DF end, v_t is the timing velocity, $\nabla n_{e,\perp}$ is the electron density gradient across the DF, and $\nabla p_{e,\perp}$ is the perpendicular electron pressure gradient across the DF.

	$v_t B_z^{max}$	$\nabla n_{e,\perp}$	$\nabla p_{e,\perp}$
$\langle P\rangle_{sig}$	0.72	0.41	0.46
$\langle P\rangle_{DF}/\langle P\rangle_{bef}$	0.25	0.17	0.13

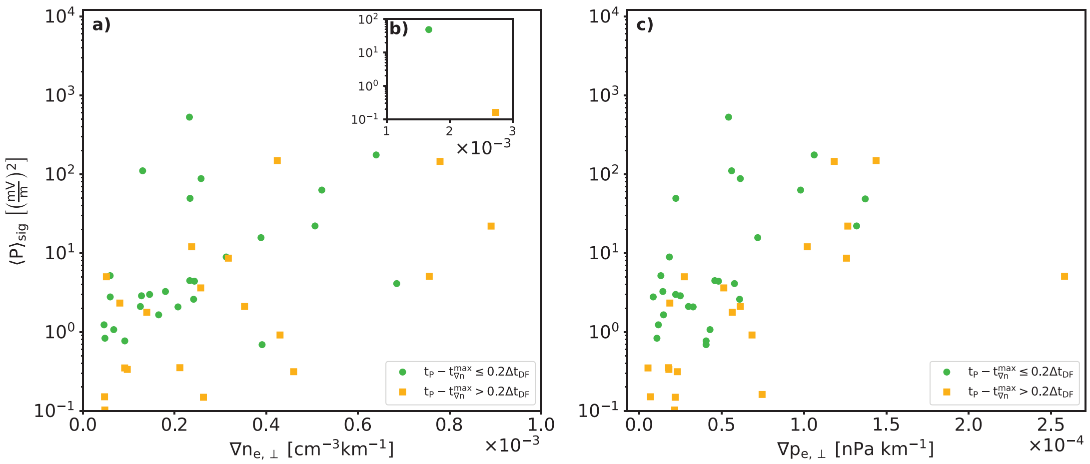

FIG. 6. (a) The relation of the electron density gradient $\nabla n_{e,\perp}$ and the average wave power during the DF, $\langle P \rangle_{\text{sig}}$. Green dots represent category 1 events, orange squares represent category 2 events. (b) Two events that exhibit much larger density gradients compared to the remaining dataset. (c) $\langle P \rangle_{\text{sig}}$ with respect to the electron pressure gradient $\nabla p_{e_\perp}$.

pressure gradients, and low wave power is only observed at weak gradients. The correlation coefficients for the power ratio before/during the DF, $\langle P \rangle_{\text{DF}}/\langle P \rangle_{\text{bef}}$, generally exhibit less correlation. A better correlation is observed when comparing $\langle P \rangle_{\text{DF}}$ with $B_z^{\max} v_t$ (0.72), as displayed in Fig. 7. The color represents the averaged $\mathbf{j} \cdot \mathbf{E}'$ value during the time window Δt_w, centered around the strongest wave power t_w [see Fig. 2(l), gray shaded area]. We observe that 11/47 (23%) events show, on average, positive values of $\mathbf{j} \cdot \mathbf{E}'$, indicating energy transfer to the electrons. On the other hand, 36/47 (77%) events show, on average, negative values, suggesting energy transfer from the electrons. Additionally, we note that strong negative values of $\mathbf{j} \cdot \mathbf{E}'$ are generally observed for larger $B_z^{\max} v_t$ (upper right corner in Fig. 7), whereas positive values are observed for both low and high values of $B_z^{\max} v_t$.

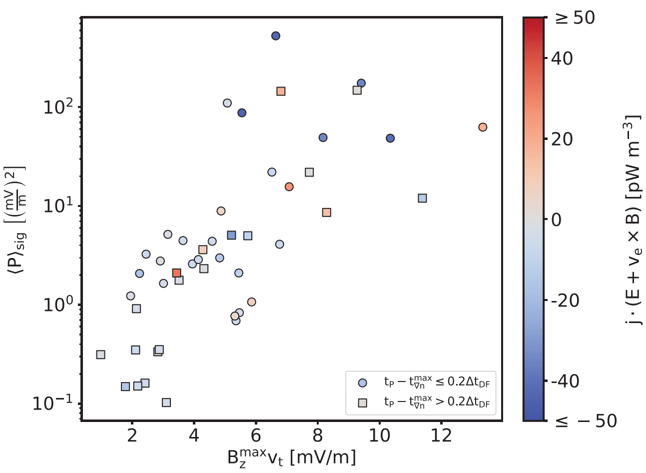

FIG. 7. Comparison of the wave power during the DF, $\langle P \rangle_{\text{sig}}$, with the z component of the magnetic field at the DF end times the timing velocity of the DF, $B_z^{\max} v_t$. The color represents $\mathbf{j} \cdot \mathbf{E}'$ in the electron frame, averaged over the time interval around the strongest wave power Δt_w.

IV. DISCUSSION

In this study, we investigate electric field fluctuations in the lower-hybrid frequency range at dipolarization fronts in the magnetotail.

Enhanced wave signatures are observed in all events for which the DF beginning/ending times are correctly determined by the automated algorithm, that is, for 53 events. In general, they are located in the middle or toward the end of the DF. The latter observation is consistent with earlier reports of a single-event observation from Khotyaintsev *et al.* (2011). Similar features were observed at the magnetopause by André *et al.* (2001) and Panov *et al.* (2006), where comparable conditions are at hand, i.e., gradients in both the magnetic field and plasma density. They reported wave signatures in the lower-hybrid frequency range toward the high-density/high-magnetic field side (magnetospheric side), which is qualitatively comparable to our observations at the DFs. However, some DF events exhibit stronger wave power than others. The range of wave power can be several orders of magnitude, as shown in Fig. 6. We hypothesize that the reason for this observation is twofold. First, we argue that for the observed events different initial plasma conditions could have led to different growth rates of the LHDI and eventual levels of saturation, resulting in different electric field fluctuation amplitudes at time of observation. Second, lower-hybrid waves can be the reason for strong plasma particle heating, where the wave energy is effectively converted to the kinetic energy of the present particles, i.e., the wave energy is, therefore, dissipated over time (Nakamura *et al.*, 2019).

All 47 events (category 1 and 2) show a density gradient across the DF front and a large part of events (category 1 events: 27/47, 57%) contained the strongest wave signature at the steepest density gradient location. In line with Nakamura *et al.* (2019), we interpret this as an indication that at such steep gradients, the LHDI growth is strongly enhanced due to increased diamagnetic currents. Here, we point out that a widely known initial work of Davidson *et al.* (1977) makes statements about the stabilizing effect of the plasma beta on the LHDI, and the observed plasma beta (1–10) at the DFs in the current study [see Fig. 2(g)] is in a range within this strong stabilization. However, it is noted that the work of Davidson *et al.* (1977) is based on assumptions such as fully unmagnetized ions and no harmonic cyclotron resonance for electrons. On the other hand, based on linear analysis in the fully kinetic regime without such restrictions, Nakamura *et al.* (2019) recently showed that the LHDI would be highly unstable at the DFs in a typical parameter range of the earth's magnetotail, including the moderately high plasma beta as listed in the current study. Theoretically, the LHDI is induced by diamagnetic currents resulting from the present density gradients, perpendicular to the background magnetic field across the boundary. However, the average density gradient generally varies in the range $(0.05 - 1) \times 10^{-3}\,\mathrm{cm}^{-3}\,\mathrm{km}^{-1}$ among the DF events and even two extreme cases with up to $2.73 \times 10^{-3}\ \mathrm{cm}^{-3}\ \mathrm{km}^{-1}$ have been identified. We hypothesize that this is caused by, first, different ambient plasma conditions around the creation site of the DF event and, second, the change in density (and pressure) gradient over time. In Schmid *et al.* (2015), it was suggested that DF events can be divided into several categories that are distinguished by whether or not the density and/or temperature across the front region changes significantly. They further argued that DF events with large density changes eventually evolve into events with much less density difference as they propagate away from the reconnection site toward the earth into more dipolar-shaped magnetic field regions. Since the location and time point of the DF's origin and wave excitation is generally unknown, a link between the elapsed time after the DF creation and the original density gradient layer profile is therefore difficult.

There exists a weak relation between the electron density and pressure gradient across the DF and the wave power, as shown in Fig. 6. However, the correlation is low and the results scatter considerably. Since the time scale of the fastest growing mode of the LHDI is on the order of seconds (Nakamura *et al.*, 2019), we hypothesize that for many events, the instability and the associated wave signatures are already observed in a nonlinear stage and a clear correlation cannot be observed. An additional factor for the growth rate of the LHDI can be the influence of magnetic field line curvature. Shinohara *et al.* (1998) presented results about the dependence of the LHDI growth rate with respect to magnetic curvature at the reconnection site, which indicates that a large field line curvature can lead to enhanced LHDI growth rates. Determining the curvature radius of the entire DF structure is unreliable due to the small S/C separation of MMS during the event observation. However, Li *et al.* (2011) estimated the curvature radius at a dipolarization front using THEMIS data (Angelopoulos, 2008) to be in the range of $1R_{\mathrm{E}}$. These results suggest that for some events of our database, the field line curvature might play a role in determining the LHDI growth rate, and, therefore, might contribute to the scatter in the observed wave power. Nonetheless, we observe that low density gradients are mainly accompanied by low wave power $[10^{-1} - 10^{1}\,(\mathrm{mV/m})^2]$ and steeper density gradients are mainly accompanied by high wave power $[10^{1} - 10^{3}\,(\mathrm{mV/m})^2]$. A similar situation is at hand regarding the relation between $\langle P\rangle_{\mathrm{sig}}$ and $\nabla p_{e,\perp}$. We identify several notable features in Fig. 6(c): first, we identify that, in general, lower wave power goes with weaker gradients (up to $\nabla p_{e,\perp} \lesssim 0.7 \times 10^{-4}$ nPa/km). We hypothesize that with small gradients, the present LHDI is not able to sustain higher-power waves. However, since we do not assume that such gradients are necessarily constant over time, waves of higher power could be created at an earlier time and dissipate away only very slowly. Second, events with stronger wave power $[10 - 1000\ (\mathrm{mV/m})^2]$ are observed up to values of $\nabla p_{e,\perp} \lesssim 1.5 \times 10^{-4}$ nPa/km. We assume that this is a direct consequence of a strong LHDI, leading to wave signatures with high power. Third, we identify no events in the parameter range of weak wave power $[<10\ (\mathrm{mV/m})^2]$, yet strong electron pressure gradients ($\nabla p_{e,\perp} \gtrsim 0.7 \times 10^{-4}$ nPa/km). We hypothesize that due to the strong pressure gradient, strong diamagnetic currents enhance the LHDI growth and events with a strong pressure gradient are always accompanied by a strong LHDI. Based on this assumption, this parameter range is expected to show no events, which is consistent with our observation. In this simple approach, the influence of the Doppler shift to the observed wave modes is ignored. The wave power in the frequency range of interest is quantified by integration of the modified power spectral density of the electric field fluctuations over a frequency interval, starting from 2 Hz up to the lower-hybrid frequency in the spacecraft frame. However, the Doppler shift can be calculated by using the DF propagation velocity v_t, determined by the timing method, and the phase velocity and propagation direction of the wave, obtained by the method by Norgren *et al.* (2012). Based on this estimation, the upper integration limit in Eq. (2) can change within a factor of two. Results of a subsequent analysis of the dependence of the wave power on the density and pressure gradients remain, however, the same.

Furthermore, we see a fairly good correlation between the wave power $\langle P\rangle_{\mathrm{sig}}$ and $B_z^{\max} v_t$ (see Fig. 7). One possible explanation might be that the DF acts as an energy conversion region, where large-scale plasma flows and small-scale phenomena such as the LHDI are coupled. In this simple picture, large magnetic flux transfer rates $B_z^{\max} v_t$ and the observed wave power $\langle P\rangle_{\mathrm{sig}}$ can be connected indirectly. Results by Wu and Shay (2012) suggested that ions can be reflected in front of the DF shortly after its creation during magnetic reconnection and they are effectively piled up before the DF. We assume that this increases the ion pressure gradients and, if quasi-neutrality can further be assumed, the electron density and pressure gradients also. We presume that $B_z^{\max} v_t$, as a measure of magnetic flux transport toward earth, is related to the density pileup shortly after the reconnection event when the observed waves started to develop. In this simple picture, $B_z^{\max} v_t$ would be a more suitable parameter to describe the role of the LHDI for the observed wave power since it is a proxy for the conditions during wave creation rather than during the observation time. Next, it is visible that the values of $\mathbf{j} \cdot \mathbf{E}'$ in the electron frame are mostly negative (for 77% of the considered events), indicating an overall energy transfer from the electrons to the field. Predominantly negative values of the $\mathbf{j} \cdot \mathbf{E}'$ term at DFs have also been reported by Panov *et al.* (2019) and by Alqeeq *et al.* (2022). It should be noted that the discussed values of $\mathbf{j} \cdot \mathbf{E}'$ are averaged values over the time interval of the wave observation Δt_w. However, within this interval they can strongly fluctuate and can have both positive and negative signatures during one event (Liu *et al.*, 2018), as visible in Fig. 4(e). Further detailed analyses have been performed by Ergun *et al.* (2018) close to the reconnection site, who have separated the $\mathbf{j} \cdot \mathbf{E}'$ term into different frequency ranges and distinguished between perpendicular and parallel directions. A statistical study about frequency-dependent $\mathbf{j} \cdot \mathbf{E}'$ contributions for a large number of DF events would be an important next step to more comprehensively understand the energy conversion processes at the DFs.

In this study, we identified the parameter ranges in which such waves can be expected and possible explanations are provided. As such, this work contributes to a better understanding of the necessary conditions for LHDI-related electric field fluctuations to develop and under which conditions they may be sustained. However, a general course of evolution of LHDI-related wave structures during a DF's life cycle is not identified because it is assumed that the initial conditions are different for each DF and also the elapsed time between creation and observation is unknown.

V. CONCLUSIONS

We summarize the observed results as follows:

- All the events show a clear wave signature within the DF. Waves are generally observed in the middle or toward the end of the front. Events show stronger wave power during the DF than before the DF.
- The time of peak wave power is temporally aligned with the time of steepest electron density gradient. Although the scatter between electron density and pressure gradient and the observed wave power is large, the results show that strong-gradient events tend to exhibit higher wave power.
- The best correlation of the wave power is found in the magnetic flux transport rate toward earth, which is a large-scale quantity.
- The power flux $\mathbf{j} \cdot \mathbf{E}'$ can show both positive and negative values, but predominantly shows negative values—indicating that in regions of strong waves, the energy from electrons is transferred to the waves.

ACKNOWLEDGMENTS

This work was supported by the Austrian Science Fund (FWF) Nos. I2016-N20, I3506-N27, and P32175-N27, by the Austrian Research Promotion Agency (FFG) Nos. 873685 and 865967, and by RSF Grant No. 18–47-05001.

AUTHOR DECLARATIONS

Conflict of Interest

The authors have no conflict of interest to disclose.

DATA AVAILABILITY

The data that support the findings of this study are openly available in the MMS Science Data Center at https://lasp.colorado.edu/mms/sdc/public/ (MMS Science Data Center), where L2 data products are provided.

NOMENCLATURE

$\langle \hat{b} \rangle$	Unit vector of the average magnetic field during the DF time interval
d_{DF}	DF thickness in km
d_i	Ion inertial length in km
$\hat{e}_\parallel$	Time-dependent unit vector, parallel to the background magnetic field
n_e, n_i	Electron and ion number density in cm^{-3}
P	Integrated wave power of the electric field fluctuations in $(\mathrm{mV})^2\mathrm{m}^{-2}$
$\langle P \rangle_{\mathrm{aft}}$	Average wave power from the time interval after the DF in $(\mathrm{mV})^2\,\mathrm{m}^{-2}$
$\langle P \rangle_{\mathrm{bef}}$	Average wave power from the time interval before the DF in $(\mathrm{mV})^2\,\mathrm{m}^{-2}$
$\langle P \rangle_{\mathrm{DF}}$	Average wave power from the time interval of the DF in $(\mathrm{mV})^2\,\mathrm{m}^{-2}$
$\langle P \rangle_{\mathrm{sig}}$	Average wave power from a time interval around t_w and duration Δt_w in $(\mathrm{mV})^2\,\mathrm{m}^{-2}$
S_m, S	(Modified) power spectral density of perp. electric field fluctuations in $(\mathrm{mV})^2\,\mathrm{m}^{-2}\,\mathrm{Hz}^{-1}$
t_P	Time of maximum wave power in s
t_r	Rescaled time vector in units of Δt_{DF}
t_w	Power-weighted average time of occurrent wave power in s
$t_{\mathrm{Bz}}^{\min}$, $t_{\mathrm{Bz}}^{\max}$	Beginning and end times of the DF in s
$t_{\nabla n}^{\max}$	Time point of steepest density gradient in s
$\lvert t_{\nabla n}^{\max} - t_P \rvert / \Delta t_{\mathrm{DF}}$	Relative temporal deviation between the time of steepest wave power and time of steepest density gradient
$\mathbf{v}_e$, $\mathbf{v}_i$	Electron and ion bulk velocity in km/s
v_t, $\mathbf{n}_t$	DF normal propagation velocity in km/s, and unit vector, obtained by the timing method
ρ_i	Ion gyroradius in km
θ	Elevation angle in degrees
Δt_{DF}	Duration of a DF event in s
$\Delta t_{\mathrm{DF}}^{\mathrm{ext}}$	$\pm 10\%$ of Δt_{DF}
Δt_w	Effective duration of occurring waves in s

REFERENCES

Alqeeq, S.. et al., "Investigation of the homogeneity of energy conversion processes at dipolarization fronts from MMS measurements," Phys. Plasmas (to be published 2022).

André, M., Behlke, R., Wahlund, J.-E., Vaivads, A., Eriksson, A.-I., Tjulin, A., Carozzi, T. D., Cully, C., Gustafsson, G., Sundkvist, D., Khotyaintsev, Y., Cornilleau-Wehrlin, N., Rezeau, L., Maksimovic, M., Lucek, E., Balogh, A., Dunlop, M., Lindqvist, P.-A., Mozer, F., Pedersen, A., and Fazakerley, A., "Multi-spacecraft observations of broadband waves near the lower hybrid frequency at the earthward edge of the magnetopause," Ann. Geophys. **19**, 1471–1481 (2001).

Angelopoulos, V., "The THEMIS mission," Space Sci. Rev. **141**, 5–34 (2008).

Angelopoulos, V., Baumjohann, W., Kennel, C. F., Coroniti, F. V., Kivelson, M. G., Pellat, R., Walker, R. J., Lühr, H., and Paschmann, G., "Bursty bulk flows in the inner central plasma sheet," J. Geophys. Res. **97**, 4027–4039, https://doi.org/10.1029/91JA02701 (1992).

Angelopoulos, V., Runov, A., Zhou, X.-Z., Turner, D. L., Kiehas, S. A., Li, S.-S., and Shinohara, I., "Electromagnetic energy conversion at reconnection fronts," Science **341**, 1478–1482 (2013).

Baumjohann, W., "Modes of convection in the magnetotail," Phys. Plasmas **9**, 3665–3667 (2002).

Baumjohann, W., Hesse, M., Kokubun, S., Mukai, T., Nagai, T., and Petrukovich, A. A., "Substorm dipolarization and recovery," J. Geophys. Res. **104**, 24995–25000, https://doi.org/10.1029/1999JA900282 (1999).

Baumjohann, W., Paschmann, G., and Lühr, H., "Characteristics of high-speed ion flows in the plasma sheet," J. Geophys. Res. **95**, 3801–3809, https://doi.org/10.1029/JA095iA04p03801 (1990).

Birn, J., Hesse, M., Nakamura, R., and Zaharia, S., "Particle acceleration in dipolarization events," J. Geophys. Res. **118**, 1960–1971, https://doi.org/10.1002/jgra.50132 (2013).
Burch, J. L., Moore, T. E., Torbert, R. B., and Giles, B. L., "Magnetospheric multiscale overview and science objectives," Space Sci. Rev. **199**, 5–21 (2016).
Cairns, I. H. and McMillan, B. F., "Electron acceleration by lower hybrid waves in magnetic reconnection regions," Phys. Plasmas **12**, 102110 (2005).
Contel, O. L., Nakamura, R., Breuillard, H., Argall, M. R., Graham, D. B., Fischer, D., Retinò, A., Berthomier, M., Pottelette, R., Mirioni, L., Chust, T., Wilder, F. D., Gershman, D. J., Varsani, A., Lindqvist, P., Khotyaintsev, Y. V., Norgren, C., Ergun, R. E., Goodrich, K. A., Burch, J. L., Torbert, R. B., Needell, J., Chutter, M., Rau, D., Dors, I., Russell, C. T., Magnes, W., Strangeway, R. J., Bromund, K. R., Wei, H. Y., Plaschke, F., Anderson, B. J., Le, G., Moore, T. E., Giles, B. L., Paterson, W. R., Pollock, C. J., Dorelli, J. C., Avanov, L. A., Saito, Y., Lavraud, B., Fuselier, S. A., Mauk, B. H., Cohen, I. J., Turner, D. L., Fennell, J. F., Leonard, T., and Jaynes, A. N., "Lower hybrid drift waves and electromagnetic electron space-phase holes associated with dipolarization fronts and field-aligned currents observed by the magnetospheric multiscale mission during a substorm," J. Geophys. Res. **122**, 12236–12257, https://doi.org/10.1002/2017JA024550 (2017).
Daughton, W., "Electromagnetic properties of the lower-hybrid drift instability in a thin current sheet," Phys. Plasmas **10**, 3103 (2003).
Davidson, R. C. and Gladd, N. T., "Anomalous transport properties associated with the lower-hybrid-drift instability," Phys. Fluids **18**, 1327–1335 (1975).
Davidson, R. C., Gladd, N. T., Wu, C. S., and Huba, J. D., "Effects of finite plasma beta on the lower-hybrid-drift instability," Phys. Fluids **20**, 301–310 (1977).
Divin, A., Khotyaintsev, Y. V., Vaivads, A., and André, M., "Lower hybrid drift instability at a dipolarization front," J. Geophys. Res. **120**, 1124–1132, https://doi.org/10.1002/2014JA020528 (2015a).
Divin, A., Khotyaintsev, Y. V., Vaivads, A., André, M., Markidis, S., and Lapenta, G., "Evolution of the lower hybrid drift instability at reconnection jet front," J. Geophys. Res. **120**, 2675–2690, https://doi.org/10.1002/2014JA020503 (2015b).
Dunlop, M. W., Balogh, A., Glassmeier, K.-H., and Robert, P., "Four-point cluster application of magnetic field analysis tools: The curlometer," J. Geophys. Res. **107**, SMP 23-1–SMP 23-14, http://dx.doi.org/10.1029/2001JA005088 (2002).
Ergun, R. E., Goodrich, K. A., Wilder, F. D., Ahmadi, N., Holmes, J. C., Eriksson, S., Stawarz, J. E., Nakamura, R., Genestreti, K. J., Hesse, M., Burch, J. L., Torbert, R. B., Phan, T. D., Schwartz, S. J., Eastwood, J. P., Strangeway, R. J., Contel, O. L., Russell, C. T., Argall, M. R., Lindqvist, P.-A., Chen, L. J., Cassak, P. A., Giles, B. L., Dorelli, J. C., Gershman, D., Leonard, T. W., Lavraud, B., Retino, A., Matthaeus, W., and Vaivads, A., "Magnetic reconnection, turbulence, and particle acceleration: Observations in the earth's magnetotail," Geophys. Res. Lett. **45**, 3338–3347, https://doi.org/10.1002/2018GL076993 (2018).
Greco, A., Artemyev, A., Zimbardo, G., Angelopoulos, V., and Runov, A., "Role of lower hybrid waves in ion heating at dipolarization fronts," J. Geophys. Res. **122**, 5092–5104, https://doi.org/10.1002/2017JA023926 (2017).
Grigorenko, E. E., Malykhin, A. Y., Shklyar, D. R., Fadanelli, S., Lavraud, B., Panov, E. V., Avanov, L., Giles, B., and Contel, O. L., "Investigation of electron distribution functions associated with whistler waves at dipolarization fronts in the earth's magnetotail: MMS observations," J. Geophys. Res. **125**, e2020JA028268, https://doi.org/10.1029/2020JA028268 (2020).
Harvey, C. C., "Spatial gradients and the volumetric tensor," in *Analysis Methods for Multi-Spacecraft Data*, edited by G. Paschmann and P. W. Daly (ESA Publications Division, Noordwijk, 1998), Chap. 12.
Huang, C., Wu, M. Y., Lu, Q. M., Wang, R., and Wang, S., "Electron acceleration in the dipolarization front driven by magnetic reconnection," J. Geophys. Res. **1020**, 1759–1765, https://doi.org/10.1002/2014JA020918 (2015).
Huang, S. Y., Zhou, M., Deng, X. H., Yuan, Z. G., Pang, Y., Wei, Q., Su, W., Li, H. M., and Wang, Q. Q., "Kinetic structure and wave properties associated with sharp dipolarization front observed by cluster," Ann. Geophys. **30**, 97–107 (2012).
Khotyaintsev, Y. V., Cully, C. M., Viavads, A., Andre, M., and Owen, C. J., "Plasma jet breaking: Energy dissipation and nonadiabatic electrons," Phys. Rev. Lett. **106**, 165001 (2011).
Khotyaintsev, Y. V., Divin, A., Vaivads, A., André, M., and Markidis, S., "Energy conversion at dipolarization fronts," Geophys. Res. Lett. **44**, 1234–1242, https://doi.org/10.1002/2016GL071909 (2017).
Krall, N. A. and Liewer, P. C., "Low-frequency instabilities in magnetic pulses," Phys. Rev. A **4**, 2094 (1971).
Lapenta, G. and Bettarini, L., "Self-consistent seeding of the interchange instability in dipolarization fronts," Geophys. Res. Lett. **38**, L11102, https://doi.org/10.1029/2011GL047742 (2011).
Le Contel, O., Leroy, P., Roux, A., Coillot, C., Alison, D., Bouabdellah, A., Mirioni, L., Meslier, L., Galic, A., Vassal, M. C., Torbert, R. B., Needell, J., Rau, D., Dors, I., Ergun, R. E., Westfall, J., Summers, D., Wallace, J., Magnes, W., Valavanoglou, A., Olsson, G., Chutter, M., Macri, J., Myers, S., Turco, S., Nolin, J., Bodet, D., Rowe, K., Tanguy, M., and de la Porte, B., "The search-coil magnetometer for MMS," Space Sci. Rev. **199**, 257–282 (2016).
Li, S.-S., Angelopoulos, V., Runov, A., Zhou, X.-Z., McFadden, J., Larson, D., Bonnell, J., and Auster, U., "On the force balance around dipolarization fronts within bursty bulk flows," J. Geophys. Res. **116**, A00I35, http://dx.doi.org/10.1029/2010JA015884 (2011).
Liang, J., Ni, B., Cully, C. M., Donovan, E. F., Thorne, R. M., and Angelopoulos, V., "Lower hybrid drift waves and electromagnetic electron space-phase holes associated with dipolarization fronts and field-aligned currents observed by the magnetospheric multiscale mission during a substorm," Ann. Geophys. **30**, 467–488 (2012).
Lindqvist, P.-A., Olsson, G., Torbert, R. B., King, B., Granoff, M., Rau, D., Needell, G., Turco, S., Dors, I., Beckman, P., Macri, J., Frost, C., Salwen, J., Eriksson, A., Åhlén, L., Khotyaintsev, Y. V., Porter, J., Lappalainen, K., Ergun, R. E., Wermeer, W., and Tucker, S., "The spin-plane double probe electric field instrument for MMS," Space Sci. Rev. **199**, 137–165 (2016).
Liu, C. M., Fu, H. S., Xu, Y., Khotyaintsev, Y. V., Burch, J. L., Ergun, R. E., Gershman, D. G., and Torbert, R. B., "Electron-scale measurements of dipolarization front," Geophys. Res. Lett. **45**, 4628–4638, https://doi.org/10.1029/2018GL077928 (2018).
Liu, J., Angelopoulos, V., Runov, A., and Zhou, X., "On the current sheets surrounding dipolarizing flux bundles in the magnetotail: The case for wedgelets," J. Geophys. Res. **118**, 2000–2020, https://doi.org/10.1002/jgra.50092 (2013).
Lu, S., Angelopoulos, V., and Fu, H., "Suprathermal particle energization in dipolarization fronts: Particle-in-cell simulations," J. Geophys. Res. **121**, 9483–9500, https://doi.org/10.1002/2016JA022815 (2016).
Lu, S., Lu, Q. M., Lin, Y., Wang, X., Ge, Y., Wang, R., Zhou, M., Fu, H., Huang, C., Wu, M., and Wang, S., "Dipolarization fronts as earthward propagating flux ropes: A three-dimensional global hybrid simulation," J. Geophys. Res. **120**, 6286–6300, https://doi.org/10.1002/2015JA021213 (2015).
Malykhin, A. Y., Grigorenko, E. E., Kronberg, E. A., Daly, P. W., and Kozak, L. V., "Acceleration of protons and heavy ions to suprathermal energies during dipolarizations in the near-earth magnetotail," Ann. Geophys. **37**, 549–559 (2019).
Malykhin, A. Y., Grigorenko, E. E., Shklyar, D. R., Panov, E. V., Contel, O. L., Avanov, L., and Giles, B., "Characteristics of resonant electrons interacting with whistler waves in the nearest dipolarizing magnetotail," J. Geophys. Res. **126**, e2021JA029440, https://doi.org/10.1029/2021JA029440 (2021).
Means, J. D., "Use of the three-dimensional covariance matrix in analyzing the polarization properties of plain waves," J. Geophys. Res. **77**, 5551–5559, https://doi.org/10.1029/JA077i028p05551 (1972).
MMS Science Data Center, see https://lasp.colorado.edu/mms/sdc/public/ for "Magnetospheric Multiscale Mission Data" (last accessed December 03, 2021).
Nagai, T. and Machida, S., "Magnetic reconnection in the near-earth magnetotail," in *New Perspectives on the Earth's Magnetotail*, Geophysical Monograph Series Vol. 105, edited by A. Nishida, D. Baker, and S. Cowley (American Geophysical Union, Washington, DC, 1998), pp. 211–224.
Nakamura, R., Baumjohann, W., Klecker, B., Bogdanova, Y., Balogh, A., Rème, H., Bosqued, J. M., Dandouras, I., Sauvaud, J. A., Glassmeier, K., Kistler, L., Mouikis, C., Zhang, T. L., Eichelberger, H., and Runov, A., "Motion of the dipolarization front during a flow burst event observed by cluster," Geophys. Res. Lett. **29**, 3-1–3-4, https://doi.org/10.1029/2002GL015763 (2002).
Nakamura, R., Baumjohann, W., Mouikis, C., Kistler, L. M., Runov, A., Volwerk, M., Asano, Y., Vörös, Z., Zhang, T. L., Klecker, B., Rème, H., and Balogh, A., "Spatial scale of high-speed flows in the plasma sheet observed by cluster,"

Geophys. Res. Lett. **31**, L09804, https://doi.org/10.1029/2004GL019558 (2004).

Nakamura, T. K. M., Nakamura, R., Baumjohann, W., Umeda, T., and Shinohara, I., "Three-dimensional development of front region of plasma jets generated by magnetic reconnection," Geophys. Rev. Lett. **43**, 8356 (2016).

Nakamura, T. K. M., Umeda, T., Nakamura, R., Fu, H., and Oka, M., "Disturbance of the front region of magnetic reconnection outflow jets due to the lower-hybrid drift instability," Phys. Rev. Lett. **123**, 235101 (2019).

Norgren, C., Viavads, A., Khotyaintsev, Y. V., and André, M., "Lower hybrid drift waves: Space observations," Phys. Rev. Lett. **109**, 055001 (2012).

Pan, D.-X., Khotyaintsev, Y. V., Graham, D. B., Vaivads, A., Zhou, X., André, M., Lindqvist, P., Ergun, R. E., Contel, O. L., Russell, C. T., Torbert, R. B., Giles, B., and Burch, J. L., "Rippled electron-scale structure of a dipolarization front," Geophys. Res. Lett. **45**, 12116–12124, https://doi.org/10.1029/2018GL080826 (2018).

Panov, E. V., Baumjohann, W., Nakamura, R., Weygand, J. M., Giles, B. L., Russell, C. T., Reeves, G., and Kubyshkina, M. V., "Continent-wide R1/R2 current system and ohmic losses by broad dipolarization-injection fronts," J. Geophys. Res. **124**, 4064–4082, https://doi.org/10.1029/2019JA026521 (2019).

Panov, E. V., Büchner, J., Fränz, M., Korth, A., Khotyaintsev, Y., Nikutowski, B., Savin, S., Fornaçon, K.-H., Dandouras, I., and Rèmee, H., "Cluster spacecraft observation of a thin current sheet at the earth's magnetopause," Adv. Space Res. **37**, 1363–1372 (2006).

Plaschke, F., Kahr, N., Fischer, D., Nakamura, R., Baumjohann, W., Magnes, W., Burch, J. L., Torbert, R. B., Russell, C. T., Giles, B. L., Strangeway, R. J., Leinweber, H. K., Bromund, K. R., Anderson, B. J., Le, G., Chutter, M., Slavin, J. A., and Kepko, E. L., "Steepening of waves at the duskside magnetopause," J. Geophys. Res. **43**, 7373–7380, https://doi.org/10.1002/2016GL070003 (2016).

Pollock, C., Moore, T., Jacques, A., Burch, J., Gliese, U., Saito, Y., Omoto, T., Avanov, L., Barrie, A., Coffey, V., Dorelli, J., Gershman, D., Giles, B., Rosnack, T., Salo, C., Yokota, S., Adrian, M., Aoustin, C., Auletti, C., Aung, S., Bigio, V., Cao, N., Chandler, M., Chornay, D., Christian, K., Clark, G., Collinson, G., Corris, T., Santos, A. D. L., Devlin, R., Diaz, T., Dickerson, T., Dickson, C., Diekmann, A., Diggs, F., Duncan, C., Figueroa-Vinas, A., Firman, C., Freeman, M., Galassi, N., Garcia, K., Goodhart, G., Guererro, D., Hageman, J., Hanley, J., Hemminger, E., Holland, M., Hutchins, M., James, T., Jones, W., Kreisler, S., Kujawski, J., Lavu, V., Lobell, J., LeCompte, E., Lukemire, A., MacDonald, E., Mariano, A., Mukai, T., Narayanan, K., Nguyan, Q., Onizuka, M., Paterson, W., Persyn, S., Piepgrass, B., Cheney, F., Rager, A., Raghuram, T., Ramil, A., Reichenthal, L., Rodriguez, H., Rouzaud, J., Rucker, A., Saito, Y., Samara, M., Sauvaud, J.-A., Schuster, D., Shappirio, M., Shelton, K., Sher, D., Smith, D., Smith, K., Smith, S., Steinfeld, D., Szymkiewicz, R., Tanimoto, K., Taylor, J., Tucker, C., Tull, K., Uhl, A., Vloet, J., Walpole, P., Weidner, S., White, D., Winkert, G., Yeh, P.-S., and Zeuch, M., "Fast plasma investigation for magnetospheric multiscale," Space Sci. Rev. **199**, 331–406 (2016).

Runov, A., Angelopoulos, V., Sitnov, M., Sergeev, V. A., Bonnell, J., McFadden, J. P., Larson, D., Glassmeier, K.-H., and Auster, U., "THEMIS observations of an earthward propagating dipolarization front," Geophys. Res. Lett. **36**, 517–525, https://doi.org/10.1029/2009GL038980 (2009).

Russell, C. T., Anderson, B. J., Baumjohann, W., Bromund, K. R., Dearborn, D., Fischer, D., Le, G., Leinweber, H. K., Leneman, D., Magnes, W., Means, J. D., Moldwin, M. B., Nakamura, R., Pierce, D., Plaschke, F., Rowe, K. M., Slavin, J. A., Strangeway, R. J., Torbert, R., Hagen, C., Jernej, I., Valavanoglou, A., and Richter, I., "The magnetospheric multiscale magnetometers," Space Sci. Rev. **199**, 189–256 (2016).

Schmid, D., Nakamura, R., Plaschke, F., Volwerk, M., and Baumjohann, W., "Two states of magnetotail dipolarization fronts: A statistical study," J. Geophys. Res. **120**, 1096–1108, https://doi.org/10.1002/2014JA020380 (2015).

Schmid, D., Volwerk, M., Plaschke, F., Nakamura, R., Baumjohann, W., Wang, G. Q., Wu, M. Y., and Zhang, T. L., "A statistical study on the properties of dips ahead of dipolarization fronts observed by MMS," J. Geophys. Res. **124**, 139–150, https://doi.org/10.1029/2018JA026062 (2019a).

Schmid, D., Volwerk, M., Plaschke, F., Nakamura, R., Baumjohann, W., Wang, G. Q., Wu, M. Y., and Zhang, T. L., "Dipolarization fronts: Tangential discontinuities? On the spatial range of validity of the MHD jump conditions," J. Geophys. Res. **124**, 9963–9975, https://doi.org/10.1029/2019JA027189 (2019b).

Sergeev, V. A., Angelopoulos, V., and Nakamura, R., "Recent advances in understanding substorm dynamics," Geophys. Res. Lett. **39**, L05101, https://doi.org/10.1029/2012GL050859 (2012).

Shinohara, I., Nagai, T., Fujimoto, M., Terasawa, T., Mukai, T., Tsuruda, K., and Yamamoto, T., "Low-frequency electromagnetic turbulence observed near the substorm onset site," J. Geophys. Res. **103**, 20365–20388, https://doi.org/10.1029/98JA01104 (1998).

Shiokawa, K., Miyashita, Y., Shinohara, I., and Matsuoka, A., "Decrease in B_z prior to the dipolarization in the near-earth plasma sheet," J. Geophys. Res. **110**, A09219, http://dx.doi.org/10.1029/2005JA011144 (2005).

Smets, R., Delcourt, D., Sauvaud, J. A., and Koperski, P., "Electron pitch angle distributions following the dipolarization phase of a substorm: Interball-tail observations and modeling," J. Geophys. Res. **104**, 14571–14581, https://doi.org/10.1029/1998JA900162 (1999).

Viberg, H., Khotyaintsev, Y. V., Vaivads, A., André, M., Fu, H. S., and Cornilleau-Wehrlin, N., "Whistler mode waves at magnetotail dipolarization fronts," J. Geophys. Res. **119**, 2605–2611, https://doi.org/10.1002/2014JA019892 (2014).

Wu, M. Y., Lu, Q. M., Volwerk, M., Vörös, Z., Zhang, T. L., Shan, L. C., and Huang, C., "A statistical study of electron acceleration behind the dipolarization fronts in the magnetotail," J. Geophys. Res. **118**, 4804–4810, https://doi.org/10.1002/jgra.50456 (2013).

Wu, P. and Shay, M. A., "Magnetotail dipolarization front and associated ion reflection: Particle-in-cell simulations," Geophys. Res. Lett. **39**, L08107, http://dx.doi.org/10.1029/2012GL051486 (2012).

Zhou, M., Ashour-Abdalla, M., Deng, X., Schriver, D., El-Alaoui, M., and Pang, Y., "THEMIS observation of multiple dipolarization fronts and associated wave characteristics in the near-earth magnetotail," Geophys. Res. Lett. **36**, L20107, https://doi.org/10.1029/2009GL040663 (2009).